Photon-induced multiple particle emissions of ^{90}Zr and ^{nat}Zr from 10 to 140 MeV

T. E. Rodrigues,[1] M. N. Martins,[1] C. Garcia,[1] J. D. T. Arruda-Neto,[1] J. Mesa,[2] K. Shtejer,[1,3] and F. Garcia[4]

[1]*Instituto de Física da Universidade de São Paulo, P. O. Box 66318, CEP 05315-970, São Paulo, Brazil*
[2]*Instituto de Biociências, Universidade Estadual de São Paulo, Botucatu, Brazil*
[3]*Center of Applied Studies for Nuclear Developments (CEADEN), Havana, Cuba*
[4]*Universidade Estadual de Santa Cruz, Ilhéus, Brazil*

A comprehensive analysis of electrodisintegration yields of protons on ^{90}Zr is proposed taking into account the giant dipole resonance, isovector giant quadrupole resonance (IVGQR), and quasideuteron contributions to the total photoabsorption cross section from 10 to 140 MeV. The calculation applies the MCMC intranuclear cascade to address the direct and pre-equilibrium emissions and another Monte Carlo-based algorithm to describe the evaporation step. The final results of the total photoabsorption cross section for ^{90}Zr and relevant decay channels are obtained by fitting the (e, p) measurements from the National Bureau of Standards and show that multiple proton emissions dominate the photonuclear reactions at higher energies. These results provide a consistent explanation for the exotic and steady increase of the (e, p) yield and also a strong evidence of a IVGQR with a strength parameter compatible with the $E2$ energy-weighted sum rule. The inclusive photoneutron cross sections for ^{90}Zr and ^{nat}Zr, derived from these results and normalized with the (e, p) data, are in agreement within 10% with both Livermore and Saclay data up to 140 MeV.

I. INTRODUCTION

The investigation of multiple particle emissions following photon-induced reactions in the intermediate energy region may reveal important features of the nature of the photoabsorption mechanism.

In a previous work, we have investigated photonuclear reactions below pion threshold via a new version of the multicollisional Monte Carlo (MCMC) intranuclear cascade model [1,2]. This version was dedicated to the quasideuteron entrance channel and incorporates important improvements, most of them related with a nonstochastic treatment for the Pauli-blocking mechanism, in comparison with previous approaches [3–6]. Neutron multiplicities and the total photoabsorption cross sections for Sn, Ce, Ta, and Pb were consistently described using the MCMC model to describe the rapid stage of the nuclear reaction plus an evaporation Monte Carlo routine, based on the Weisskopf statistical theory, to address the de-excitation of the compound nucleus (CN) in terms of the competition between particle evaporation and nuclear fission. For details see Ref. [1] and references therein.

The MCMC cascade has also been useful to calculate angular distributions of mesons produced via incoherent nuclear excitation processes [7]. In this work, we have reproduced quite successfully recent data from the Mainz Microton collaboration (MAMI) for the differential cross sections for incoherent π^0 photoproduction at the $\Delta(1232)$ resonance energy region, for both ^{12}C and ^{208}Pb [8]. Also we have calculated the angular distributions of neutral pions at higher energies, typically 4.0 to 6.0 GeV, and extreme forward angles ($\theta_\pi^{lab} \lesssim 4°$) to estimate the nuclear background in the high-precision particle-production experiment carried out by the PrimEx Collaboration [9] at the Jefferson Laboratory. For details, see Ref. [7] and references therein.

In this work, we present various applications for the intranuclear and evaporation cascade Monte Carlo routines to address multiple particle emission in ^{90}Zr and Zirconium isotopes below pion threshold. The aim of the present analysis is to provide a consistent interpretation for the exotic behavior of the proton yields from the electrodisintegration of ^{90}Zr at intermediate energies [10]. The yields present a steady increase up to 130 MeV, suggesting that multiple-particle emissions are probably dominating the dynamics of the intranuclear cascade processes triggered by the quasideuteron channel.

Decay channels of ^{90}Zr in the GDR region are calculated in detail to establish the shape and magnitude of the total photoabsorption cross section up to pion threshold. The analysis takes into account the complimentary data set of proton emissions from the National Bureau of Standards (NBS) [10] and the photoneutron cross section measurements performed in Livermore [11] and Saclay [12]. Additionally, we plan to investigate possible contributions from the isovector giant quadrupole resonance (IVGQR) decay in both the electron- and photon-induced reaction processes. Such contribution was evident from the analysis of the angular distributions of γs emitted in the inverse reaction ^{89}Y$(\vec{p}, \gamma)^{90}$Zr [13].

Finally, the partial and total photoneutron cross sections from natural Zirconium [14] are evaluated up to 140 MeV. These channels represent the major contribution to the total photoabsorption cross section, and they should be included in present analysis to provide a complete description of the reaction mechanisms in this mass range.

The article is organized as follows: In Sec. II, we present an overview of the MCMC model and show the improvements both in the intranuclear and evaporation routines. In Sec. III, we discuss the character of the photonucleus interaction, evaluating the GDR and IVGQR decay modes, as well as the quasideuteron channel up to 140 MeV.

In Sec. IV the results of the calculation are presented and compared with the available experimental data. The electrodisintegration yields are evaluated using the virtual photon exchange formalism, with the related photon spectra being calculated in distorted-wave Born approximation (DWBA) [15] taking into account the nuclear charge and the nuclear finite size. In this section we propose a fitting of the (e, p) yield of ^{90}Zr, extracting the relative strengths for the GDR and IVGQR. Such approach provides a consistent method to determine the total photoabsorption cross section. The conclusions and final remarks are presented in Sec. V.

II. THE MCMC PLUS EVAPORATION APPROACH: REVIEW AND IMPROVEMENTS

A. The multicollisional intranuclear cascade model

The intranuclear cascade model MCMC consists of a sophisticated Monte Carlo routine describing the fast stage of the nuclear reactions in terms of successive binary collisions. During the time span of the binary scatterings, the remaining particles are supposed not to interact and the collisional term between the interacting particles inside the nuclear matter is approximated by the same quantity predicted for the vacuum. The basic concepts of the present calculation were first developed to study high-energy photonuclear reactions [3–6]. Although these versions have presented satisfactory results, they also had some inherent limitations related with the stochastic treatment of the Pauli-blocking mechanism and the incorporation of ambiguous quantities, such as *stopping time* parameters to determine the pre-equilibrium stage. These problems were also present in other similar models, like the Liege INC model [16], consistently overcome in a recent version of the MCMC dedicated to the quasideuteron doorway state [1]. In this regard, the present analysis applies the same version of the MCMC cascade reported in Ref. [1], with the following improvements: (i) the incorporation of realistic binding energies for the target nucleus during the evaluation of the nuclear potential and the nucleon effective masses; (ii) an accurate calculation of the energy balance during particle emissions, taking into account the actual (instantaneous) momentum distribution of the excited ensemble, instead of a predetermined Fermi-Dirac distribution used in the previous version; (iii) the evaluation of the Coulomb barrier penetrability in terms of the WKB approximation; and (iv) the calculation of the Levinger parameter in the quasideuteron model.

B. The evaporation Monte Carlo model

The evaporation stage is calculated applying the statistical theory proposed by Weisskopf [17]. The decay of the CN takes into account all accessible channels, with the related branchings calculated in terms of the nuclear level densities of the daughter nuclei. The basic steps to calculate the relative probabilities between the competing channels (particle evaporation and nuclear fission) are described elsewhere [1,18,19]. Even though these approaches have successfully described neutron multiplicities and photofission probability, they were also characterized by an oversimplification for the evaluation of the kinetic energies of the emitted particles, which were arbitrarily fixed at 2.0 MeV. Additionally, the emission of charged particles did not include any effect from the Coulomb barrier, with the outgoing charged particle kinetic energies being calculated always above the barrier. These inconsistencies are not much relevant while evaluating the neutron emission channels and the fission mechanisms in actinide nuclei, because these processes largely dominate the CN decay, with most of the emitted neutrons having kinetic energies close to 2 MeV. However, for charged particle emission − the aim of the present analysis − one has to consider the emission probability of particles with higher kinetic energies and also the Coulomb barrier penetrability. Such evaluation can be performed via the inclusion of a different approach to calculate the relative probability of all the competing channels.

The ratio between the width for the evaporation of a k particle and the neutron decay width can be written as:

$$\frac{\Gamma_k}{\Gamma_n} = \left(\frac{\gamma_k}{\gamma_n}\right) \left(\frac{E_k^*}{E_n^*}\right) \left(\frac{a_k}{a_n}\right) \exp\{2[(a_k E_k^*)^{\frac{1}{2}} - (a_n E_n^*)^{\frac{1}{2}}]\},$$

$$(1)$$

where the factors γ_k/γ_n depend on the type of the emitted particles and were taken as $\gamma_k/\gamma_n = 1$ (protons), $= 2$ (alphas), $= 1$ (deuterons), $= 3$ (tritons), and $= 2$ (^{3}He) [20]. The residual excitation energies of the daughter nuclei $E_{k(n)}^*$ depend on the total excitation energy available E^*, the binding energies $B_{k(n)}$, and the asymptotic kinetic energies $T_{k(n)}$ of the emitted particles: $E_{k(n)}^* = E^* - B_{k(n)} - T_{k(n)}$. The binding energies and neutron level density parameters (a_n) were taken from Ref. [1], taking into account shell-model corrections [21]. The ratio between the neutron and k-particle level density parameters is generally energy independent $a_k/a_n \approx r_k$, with the corresponding r_k being given by Ref. [20].

Because the neutron emission width is arbitrarily normalized to unit, we can calculate the probability of k-particle emission using the formula:

$$\frac{\Gamma_k}{\Gamma_T} = \frac{\frac{\Gamma_k}{\Gamma_n}}{1 + \sum_{i \neq n} \frac{\Gamma_i}{\Gamma_n}},$$

$$(2)$$

where the sum goes over all possible decay channels except the neutron emission.

The tunneling of the Coulomb barrier is calculated in terms of the particle's kinetic energies T_k and the Coulomb barriers V_k using the standard WKB approximation. The kinetic energies of the emitted particles range from 0 to $E^* - B_k$, where $T_k = E^* - B_k$ corresponds to the decay of the CN to the ground state of the daughter nuclei. However, the decay probability depends exponentially on the factor $(a_k E_k^*)^{\frac{1}{2}}$, which decreases as T_k increases. This relationship between Γ_k/Γ_n and T_k for a given T_n dictates the particle-energy spectra for neutral particles. The distribution of kinetic energies for charged particles should be similar but suppressed at lower energies and with the maximum shifted for higher

energies. So to achieve the proper constraint between the nuclear decay process and the Coulomb barrier penetrability, we adopted the following sampling procedure: first, the kinetic energies of the emitted particles are distributed uniformly and independently in the range from 0 to $E^* - B_k$. Then, the decay branchings are calculated with Eq. (1) and normalized with Eq. (2). These probabilities are then multiplied by penetrability factors − charged particles only − that depend on the sampled kinetic energy T_k. After this procedure, the corresponding probabilities are renormalized and the choice of the decay channel is made. Such procedure ensures that the emission process is described in terms of a joint probability between a nuclear de-excitation mechanism [Eq. (1)] and a Coulomb penetrability factor.

In fact, this new approach satisfactorily includes the Coulomb tunneling and provides a more rigorous formalism to address the nuclear evaporation step. In previous models, the effect of the Coulomb barrier was artificially included in the evaluation of the residual excitation energy E_k^*, which was calculated subtracting the Coulomb barrier and assuming a fixed value for T_k. This arbitrary decrease in E_k^* also decreases the emission probability Γ_k/Γ_n in an attempt to mimic the suppression of charged-particle emission. Another direct consequence of such arbitrary procedure is its inability to predict charged-particle energy spectra, because T_k is held fixed and always above the barrier.

III. PHOTOABSORPTION MECHANISMS BELOW PION THRESHOLD

The nuclear photoabsorption mechanisms are largely dominated by collective excitations below approximately 30 MeV, with the giant dipole resonance (GDR) representing the major contribution for the nuclear strength function. Other multipole resonances have also been measured [13,22] and predicted by microscopic random-phase approximation (RPA) using a density-dependent particle-hole force [23]. However, the quasideuteron (QD) channel dominates the total photoabsorption cross section in the 40- to 140-MeV range. This model assumes that the incoming photon interacts with a neutron-proton pair embedded in the nuclear matter [24] and was described in detail in a previous article [1].

For intermediate and heavy nuclei, the direct and pre-equilibrium emissions represent a small contribution at lower energies and the memory from the initial nuclear excitation is vanished when the system achieves a thermally equilibrated state, namely the CN stage. We showed in a recent article that direct particle emissions from the GDR decay play a small contribution (below 10%) in an intermediate nuclei such as ^{64}Zn [25] and should also contribute with a small fraction for ^{90}Zr and ^{nat}Zr. Such contribution can be estimated by the analysis of the proton energy spectrum at lower energies obtained by the NBS [10], which clearly shows the contribution of narrow peaks, corresponding to well-known excited states of ^{89}Y, and a much larger evaporation-like background. For this reason, we have neglected direct and semidirect particle emission within the GDR energy region. It is worth mentioning, however, that due to kinematical

considerations these nonresonant processes play an essential role in the inverse reaction ^{89}Y(p, γ), as pointed out elsewhere [13,26]. For this reason, the specific multipolarity of the photoabsorption mechanism, dictated by the angular momentum transferred by the incoming photon, is not very relevant for the evaluation of the nuclear reaction, as far as a collective nuclear excitation dominates the photoabsorption mechanism. The differential cross sections, for instance, are largely dominated by the evaporation stage, making it very difficult to disentangle possible angular correlations from the initial photon-nucleus interaction. For lighter nuclei, however, measurements of the angular distributions of the emitted particles may reveal the dominant character of the photoabsorption mechanism and also possible interferences between different vibrational modes.

In this regard, probing the nucleus with electrons may be an adequate approach to extract the nuclear response for resonances with higher multipolarities due to the enhancement of the virtual photon spectra with $l = 2$ in comparison with the dominating $l = 1$ contribution. Consequently, the analysis of electrodisintegration yields, like the measurements performed at the NBS for proton emission on ^{90}Zr [10], may provide an efficient approach to disentangle the relative strengths of the IVGQR and the GDR at lower energies.

The total photoabsorption cross section up to pion threshold can be written in terms of the three major contributions:

$$\sigma_{\gamma,\text{abs}}(\omega) = C_0\sigma_{\text{GDR}}(\omega) + C_1\sigma_{\text{IVGQR}}(\omega) + \sigma_{\text{QD}}(\omega), \quad (3)$$

where $C_0\sigma_{\text{GDR}}$, $C_1\sigma_{\text{IVGQR}}$, and σ_{QD} represent, respectively, the GDR, IVGQR, and QD contributions. The shapes of the GDR and IVGQR are generally written in terms of Lorentz curves, with the QD part calculated via the usual expression:

$$\sigma_{\text{QD}}(\omega) = \frac{L}{A}\text{NZ}\sigma_D(\omega)f(\omega), \quad (4)$$

with

$$L = \frac{3(1 - \alpha\text{r}_{\text{eff}})}{2r_0^3\alpha}\int_0^{k_F} 24\frac{k^2}{k_F^3}\left[1 - \frac{3k}{2k_F}\right.$$
$$\left. + \frac{1}{2}\left(\frac{k}{k_F}\right)^3\right]\frac{1}{\alpha^2 + k^2}dk, \quad (5)$$

where $\sigma_D(\omega)$ is the deuteron photodisintegration cross section and $f(\omega)$ the Pauli-blocking function calculated from the MCMC routine [1]. The values of the relevant constants α, r_{eff} and the Fermi momentum k_F were taken from Ref. [1], except for the r_0 parameter taken here as 1.25 fm. The Eq. (4) and (5) propitiate the calculation of the QD contribution and assume that the nucleon momentum distribution at the ground state is that of a Fermi distribution without N-N correlations. The Levinger parameter obtained for ^{90}Zr within this approximation is $L = 5.9$, which is in fair agreement with previous calculations [27].

The photoneutron cross section measurements of ^{90}Zr in the GDR region performed at Livermore [11] and Saclay [12] show that the GDR peaks are satisfactorily reproduced by Lorentz shapes. However, the fitted curves overestimate/underestimate the data at lower/higher energies, introducing artificial tails

for the GDR. The shape of the total photoabsorption cross section [Eq. (3)] should be calculated precisely in the whole energy region. For this reason, we have adopted a consistent and alternative procedure to delineate the shape of $\sigma_{\gamma,\text{abs}}$ in the GDR region by the combination of the experimental photoneutron yields and the particle emission branching ratios calculated in the MCMC plus evaporation framework. In this procedure, the total photoabsorption cross section $\sigma_{\gamma,\text{abs}}$ is written as:

$$\sigma_{\gamma,\text{abs}}(\omega) = C_2 \sigma_{\gamma,\text{abs}}^{\text{Exp}}(\omega) = C_2 \frac{\sigma_{\gamma,\text{Sn}}(\omega)}{\sum_{x,y} x \Gamma_{\gamma,\text{xnyp}}(\omega)}, \quad (6)$$

where $\sigma_{\gamma,\text{Sn}}(\omega)$ is the photoneutron yield and $\Gamma_{\gamma,\text{xnyp}}(\omega)$ the branching ratio for the emission of x neutrons and y protons from the nuclei. The sum goes up to $x = y = 3$ in the GDR region. The photoneutron yields were measured by various groups, where we have concentrated our analysis on the measurements performed at Livermore and Saclay. These data were obtained using monochromatic photons and are consistent with each other within a global normalization factor of approximately 1.16. In fact, previous works have reported systematic discrepancies between the absolute values obtained at Livermore and Saclay [25,28] making it difficult to establish the absolute value for $\sigma_{\gamma,\text{Sn}}(\omega)$. However, the shapes of the cross sections obtained at Livermore and Saclay for ^{90}Zr are in fair agreement in the GDR region, even though the Saclay data exhibit higher fluctuations. For this reason, we have adopted the Livermore data as the input for Eq. (6), allowing a global normalization constant C_2 to be determined by the NBS results [10].

For the IVGQR we have used a Breit-Wigner formula [29] times ω^{2l-1} to account for the multipolarity of the radiation absorbed by the nucleus ($l = 2$). So, the IVGQR component can be written as:

$$\sigma_{\text{IVGQR}}(\omega) = 4.115 \times 10^{-5} \omega^3 \sigma_{\text{BW}}(\omega), \quad (7)$$

with

$$\sigma_{\text{BW}}(\omega) = \frac{\left(\frac{\Gamma}{2}\right)^2}{(\omega - \omega_0)^2 + \left(\frac{\Gamma}{2}\right)^2}. \quad (8)$$

The factor 4.115×10^{-5} was arbitrarily introduced to normalize the peak of σ_{IVQR} to 1 mb. The resonance parameters were taken as $\omega_0 = 28.5$ MeV and $\Gamma = 8.5$ MeV, which are consistent with the values reported in Ref. [13]. A Lorentz tail $\sigma_L(\omega)$ was taken for the IVGQR to ensure its convergence to zero at higher energies. Although being completely arbitrary, such particular choice for the tail of σ_{IVGQR} does not introduce a significant systematic uncertainty in the relevant observables, as will be presented in the following section. Indeed, taking two distinct exponential tails for σ_{IVGQR} has little influence on the final results, which are more sensitive to the statistical uncertainty of the strength parameter C_1. The shape of the σ_{IVGQR} and the corresponding Lorentz and exponential tails are shown in Fig. 1.

With this approach, we may write Eq. (3) in the form:

$$C_0 \sigma_{\text{GDR}}(\omega) = C_2 \sigma_{\gamma,\text{abs}}^{\text{Exp}}(\omega) - C_1 \sigma_{\text{IVGQR}}(\omega) - \sigma_{\text{QD}}(\omega). \quad (9)$$
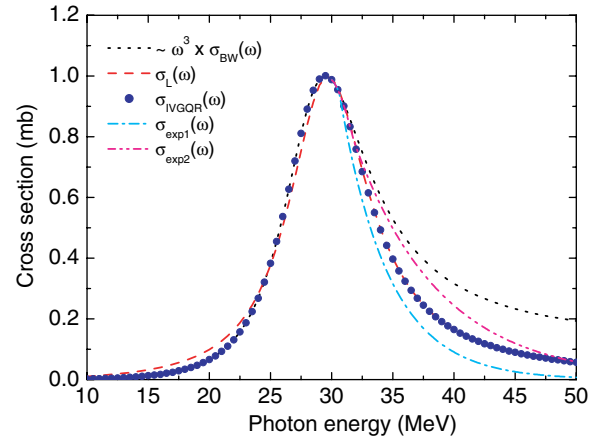

FIG. 1. (Color online) Shape of the IVGQR (blue circles). The dotted black line is proportional to $\omega^3 \times \sigma_{\text{BW}}(\omega)$, the dashed red line to $\sigma_L(\omega)$, with the dashed-dotted cyan and dashed-double-dotted magenta lines representing two distinct exponential tails for the IVGQR. Details in the text.

The constants C_1 and C_2 completely determine the total photoabsorption cross section and will be obtained in the next section combining the accurate measurements of electrodisintegration yields for proton emission on ^{90}Zr and the branching ratios calculated in the Monte Carlo routine. Indeed, the nuclear electroexcitation via virtual photons enhances the $E2$ strength due to the corresponding increase in the virtual photon spectra with $l = 2$.

IV. RESULTS

A. Particle-emission branching ratios

This section presents the results of particle-emission branching ratios from neutron threshold up to 140 MeV via the coupling of the time-dependent intranuclear cascade model MCMC and the evaporation code. The direct and pre-equilibrium emissions are evaluated for QD events generating CN configurations that are recorded to feed the evaporation routine. The GDR and IVGQR decay are calculated with the evaporation code under the assumption that the photon energy is completely absorbed by the nucleus and no direct emission takes place. The evaporation phase was calculated for ^{90}Zr, ^{91}Zr, ^{92}Zr, and ^{94}Zr from neutron threshold up to 30 MeV, in 1 MeV steps, in order to delineate with high statistics the competing processes near the nuclear giant resonances considered in this paper.

The results for the branching ratios for the emission of x neutrons and y protons at lower energies, $\Gamma_{\gamma,\text{xnyp}}^R$, are presented in Fig. 2 for ^{90}Zr, where the label R indicates that these quantities refer to resonance (GDR or IVGQR) decay only. The arrows show the theoretical values of the binding energies B_{1n} and B_{2n}, which are fairly reproduced in the present calculations. The steep increase of the (γ, n) channel at approximately 12 MeV indicates that the neutron channel is highly favorable at lower energies due to the Coulomb suppression for the (γ, p) channel. The (γ, p)
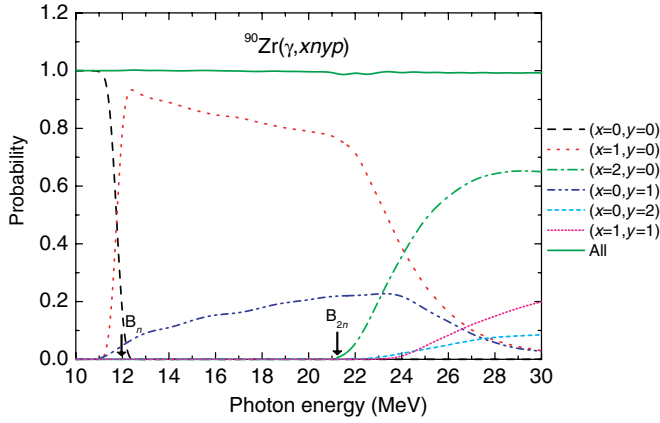
FIG. 2. (Color online) Branching ratios of ^{90}Zr (evaporation only) from 10 to 30 MeV. $\Gamma^R_{\gamma,0n0p}$(dashed black), $\Gamma^R_{\gamma,1n0p}$(dotted red), $\Gamma^R_{\gamma,2n0p}$(dashed-dotted green), $\Gamma^R_{\gamma,0n1p}$(dashed-double-dotted blue), $\Gamma^R_{\gamma,0n2p}$(short-dashed cyan), and $\Gamma^R_{\gamma,1n1p}$(short-dotted magenta). The sum off all channels is represented by the solid olive line.

channel width, however, presents a soft increase up to 23 MeV, reaching approximately 17% at the GDR peak. Other channels involving the emission of two particles become favorable above approximately 22 MeV. The sum of all channels is presented for consistency.

Multiple-particle emission following intermediate energy photoabsorption were calculated taking into account the pre-equilibrium stage in the energy range from 20 to 140 MeV. Below 20 MeV, the pre-equilibrium emissions are negligible and the QD channel is not distinguishable from the pure evaporation stage. The complete (cascade+evaporation) branching ratios are calculated in the form:

$$\Gamma^{QD}_{\gamma,xnyp} = \sum_{i=0}^{x}\sum_{j=0}^{y}[\Gamma_{\gamma,(x-i)n(y-j)p}]_C \times (\Gamma_{\gamma,injp})_{evap}, \quad (10)$$

where $[\Gamma_{\gamma,(x-i)n(y-j)p}]_C$ is the probability of formation of the CN configuration $[(x-i)n,(y-j)p]$ at a given excitation energy and $(\Gamma_{\gamma,injp})_{evap}$ the probability of evaporation of i neutrons and j protons for the corresponding CN configuration. The first branchings $[\Gamma_{\gamma,(x-i)n(y-j)p}]_C$ and the corresponding excitation energies are calculated in the MCMC framework and are the basic ingredients to run the evaporation code to achieve $(\Gamma_{\gamma,injp})_{evap}$. The results for the branchings for ^{90}Zr are presented in Fig. 3 for $0 \leqslant x \leqslant 7$ and $0 \leqslant y \leqslant 3$. It is worth noticing, however, that decay channels with two protons are more favorable than with only one for energies above approximately 80 MeV. In fact, the channels $(\gamma, 3n2p)$, $(\gamma, 4n2p)$, and $(\gamma, 5n2p)$ represent the major contributions for energies above 120 MeV.
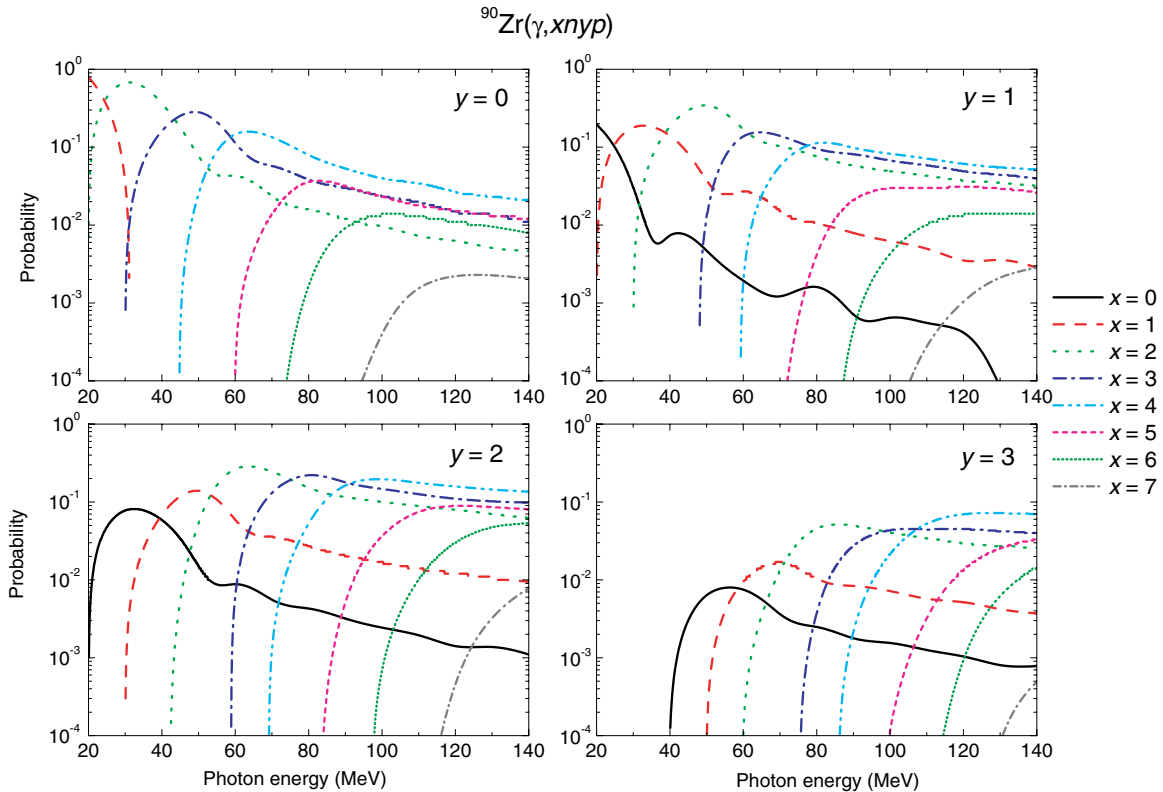

FIG. 3. (Color online) Branching ratios (cascade+evaporation) of ^{90}Zr$(\gamma, xnyp)$ from 20 to 140 MeV. (Upper left panel) $\Gamma^{QD}_{\gamma,0n0p}$ (solid black), $\Gamma^{QD}_{\gamma,1n0p}$(dashed red), $\Gamma^{QD}_{\gamma,2n0p}$(dotted green), $\Gamma^{QD}_{\gamma,3n0p}$(dashed-dotted blue), $\Gamma^{QD}_{\gamma,4n0p}$(dashed-double-dotted cyan), $\Gamma^{QD}_{\gamma,5n0p}$(short-dashed magenta), $\Gamma^{QD}_{\gamma,6n0p}$(short-dotted olive), and $\Gamma^{QD}_{\gamma,7n0p}$(short-dashed-dotted gray). (Upper right panel) The same with $y = 1$. (Lower left panel) The same with $y = 2$. (Lower right panel) The same with $y = 3$.
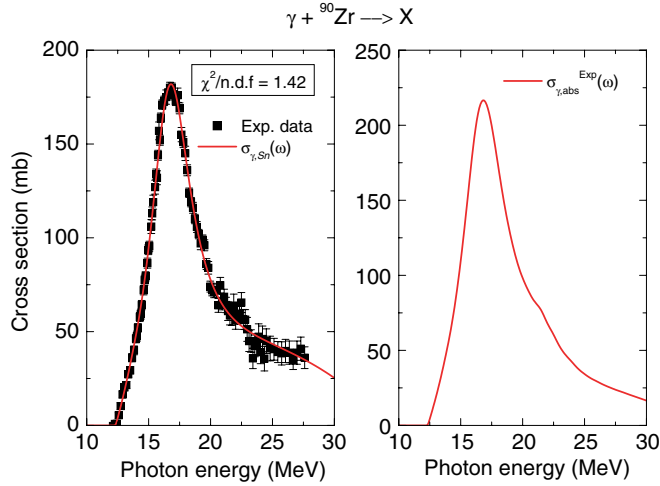
FIG. 4. (Color online) (Left panel) Total photoneutron yield of ^{90}Zr [11] (data points) and the corresponding fitted cross section $\sigma_{\gamma,Sn}(\omega)$ (red line). (Right panel) $\sigma_{\gamma,abs}^{Exp}(\omega)$ [see Eq. (6)].

B. Total photoabsorption cross section on ^{90}Zr via the analysis of the (e, p) channel.

This section aims to calculate the total photoabsorption cross section for ^{90}Zr by combining the photoneutron [11] and electrodisintegration experimental yields [10] of ^{90}Zr and the branchings calculated in the MCMC plus evaporation routines.

The first step of our analysis is the determination of $\sigma_{\gamma,abs}^{Exp}(\omega)$ [Eq. (6)] by a fitting of the photoneutron yield from Livermore [11]. The fitted curve was assumed to be a combination of a Lorentz shape, with the parameters given by Ref. [30], and a polynomial function of ω to account for the discrepancies at the lower and higher energy ranges. The specific form of the fitted function is not relevant, insofar as it accurately describes the data in the energy range considered. The fitting curve $\sigma_{\gamma,Sn}(\omega)$ and the corresponding data set [11] are shown in the left panel of Fig. 4, with the calculated function $\sigma_{\gamma,abs}^{Exp}(\omega)$ [see Eq. (6)] in the right panel.

The electrodisintegration yield for proton emission can be written in terms of the corresponding photoproton yield via the virtual photon formalism [31]:

$$\sigma_{e,Sp}(E_e) = \sum_{\lambda l} \int_{B_p}^{Ee} \frac{d\omega}{\omega} S^{\lambda l}(E_e, \omega) \sigma_{\gamma,Sp}^{\lambda l}(\omega), \qquad (11)$$

where E_e is the incident electron energy, λl the multipolarity of the radiation absorbed by the nucleus, and $S^{\lambda l}(E_e, \omega)$ the corresponding virtual photon spectrum. The virtual photon spectra were calculated in distorted-wave Born approximation (DWBA) [15] taking into account the nuclear charge and finite size. The photoproton yield $\sigma_{\gamma,Sp}(\omega)$ can be written in terms of the three major contributions considered in this article:

$$\sigma_{\gamma,Sp}(\omega) = \left[C_0 \sigma_{GDR}^{E1}(\omega) + C_1 \sigma_{IVGQR}^{E2}(\omega) \right] \\ \times \Gamma_{\gamma,Sp}^{R}(\omega) + \sigma_{QD}^{E1}(\omega) \times \Gamma_{\gamma,Sp}^{QD}(\omega), \qquad (12)$$

because the $E1$ radiation dominates the GDR and QD mechanisms, whereas the IVGQR component has multipolarity $E2$ (the labels $E1$ and $E2$ are omitted from now on). The quantity

$\Gamma_{\gamma,Sp}^{R}(\omega)$ is the total photoproton branching related with a resonance (GDR/IVGQR) decay and $\Gamma_{\gamma,Sp}^{QD}(\omega)$ is the same for the QD channel, where the direct and pre-equilibrium emissions are taken into account. These branchings can be written as:

$$\Gamma_{\gamma,Sp}^{R(QD)}(\omega) = \sum_x \sum_y y \Gamma_{\gamma,xnyp}^{R(QD)}(\omega), \qquad (13)$$

where the y sum goes from 0 to 4 and the x sum goes from 0 to 10.

Inserting Eq. (12) into Eq. (11) and using Eq. (9), we have after some algebra:

$$\begin{aligned} \sigma_{e,Sp}(E_e) &= C_2 \int_{B_p}^{Ee} \frac{d\omega}{\omega} S^{E1}(E_e, \omega) \Gamma_{\gamma,Sp}^{R}(E_e, \omega) \sigma_{\gamma,abs}^{Exp}(\omega) \\ &+ C_1 \int_{B_p}^{Ee} \frac{d\omega}{\omega} [S^{E2}(E_e, \omega) - S^{E1}(E_e, \omega)] \\ &\times \Gamma_{\gamma,Sp}^{R}(\omega) \sigma_{IVGQR}(\omega) \\ &+ \int_{B_p}^{Ee} \frac{d\omega}{\omega} S^{E1}(E_e, \omega) \\ &\times \left[\Gamma_{\gamma,Sp}^{R}(\omega) - \Gamma_{\gamma,Sp}^{QD}(\omega) \right] \sigma_{QD}(\omega). \end{aligned} \qquad (14)$$

The QD component is known in shape and magnitude [Eqs. (4) and (5)]. So, we can write:

$$\begin{aligned} \tilde{\sigma}_{e,Sp}(E_e) &= \sigma_{e,Sp}(E_e) - \int_{B_p}^{Ee} \frac{d\omega}{\omega} S^{E1}(E_e, \omega) \\ &\times \left[\Gamma_{\gamma,Sp}^{R}(\omega) - \Gamma_{\gamma,Sp}^{QD}(\omega) \right] \sigma_{QD}(\omega) \\ &= C_2 \int_{B_p}^{Ee} \frac{d\omega}{\omega} S^{E1}(E_e, \omega) \Gamma_{\gamma,Sp}^{R}(E_e, \omega) \sigma_{\gamma,abs}^{Exp}(\omega) \\ &+ C_1 \int_{B_p}^{Ee} \frac{d\omega}{\omega} [S^{E2}(E_e, \omega) - S^{E1}(E_e, \omega)] \\ &\times \Gamma_{\gamma,Sp}^{R}(\omega) \sigma_{IVGQR}(\omega). \end{aligned} \qquad (15)$$

The constants C_1 and C_2 are then determined using the experimental results for the electro-disintegration proton yield $\sigma_{e,Sp}(E_e)$ from the NBS [10]. However, because the contributions $C_0 \sigma_{GDR}(\omega)$ and $C_1 \sigma_{IVGQR}(\omega)$, which are ingredients of Eq. (12), depend on the values of the constants C_1 and C_2 [see Eq. (9)], it is necessary to perform an iterative procedure to disentangle the IVGQR contribution for the total photoabsorption cross section. Such a procedure is accomplished inserting the fitted values of C_1 and C_2 into Eqs. (9) and (12) and repeating the fitting for Eq. (15). The iterative method finishes when the values of C_1 and C_2 converge satisfactorily. The results of the fitting are presented in Fig. 5 together with the data of Ref. [10]. The values of the constants $C_1 = 9.7(22)$ and $C_2 = 1.094(11)$ uniquely define the total photoabsorption cross section, with C_2 representing an approximate normalization factor between the NBS and Livermore data. The corresponding photoproton yield $\sigma_{\gamma,Sp}(\omega)$ is then calculated via Eq. (12). The results and the corresponding contributions of the GDR, IVGQR, and QD are shown in left panel of Fig. 6.
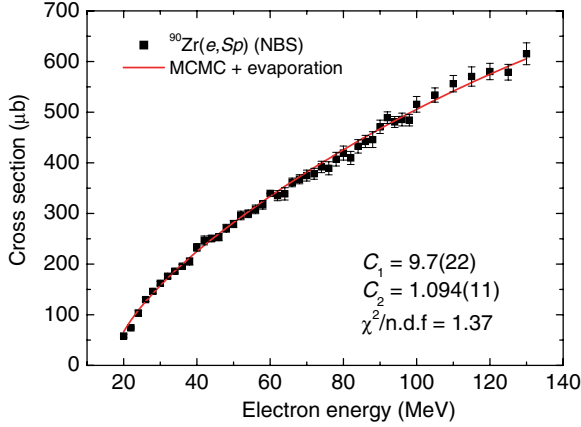
FIG. 5. (Color online) Electrodisintegration proton yield measured at the NBS [10] (data points) and the corresponding fitting function [see Eq. (15)] proposed in this work. Details in the text.

The strength of IVGQR can be verified calculating the isovector $E2$ energy-weighted sum rule (EWSR) given by [13]:

$$
\begin{aligned}
S_{\text{th}} &= \int_0^\infty \frac{\sigma(\omega)}{\omega^2} d\omega \\
&= \frac{\pi^2}{5Mc^2} \frac{e^2}{\hbar c} \frac{NZ}{A} R^2 \\
&= 0.11 \text{mb/MeV},
\end{aligned} \tag{16}
$$

where we have used $r_0 = 1.25$ fm. The corresponding value for the EWSR obtained with the constant C_1 gives $S_{\text{exp}} = 0.121(29)$ mb/MeV, which is in good agreement with the prediction from theory. The quoted error of S_{exp} was calculated adding in quadrature statistical ($\sim 20\%$) and systematic ($\sim 9\%$) parts. The statistical error comes from the fitted constant C_1, and the systematic contribution was estimated using different exponential tails for σ_{IVGQR}, refitting the constant C_1, and
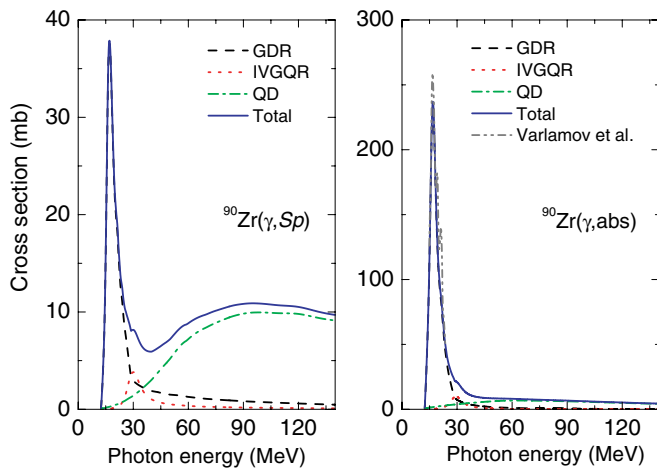

FIG. 6. (Color online) (Left panel) Total photoproton yield on ^{90}Zr (solid blue) and corresponding contributions of the GDR (dashed black), IVGQR (dotted red), and QD (dashed-dotted green). (Right panel) Total photoabsorption cross section on ^{90}Zr and corresponding contributions (same as in left panel). The dashed-double-dotted gray line indicates the compilation of Ref. [32].

recalculating S_{exp}. In fact, the constraint imposed by Eq. (15) leads to a strong correlation between the constant C_1 and the tail of σ_{IVGQR} to keep the integral unchanged. However, taking the exponential tails 1 and 2 for σ_{IVGQR} (see Fig. 1) does not affect S_{exp} considerably due to the factor $\frac{1}{\omega^2}$. S_{exp} ranges from 0.116 mb/MeV to 0.137 mb/MeV when the exponential tails 1 and 2 are used, respectively. It is interesting to point out that the generally observed enhancement factor of the $E1$ sum rule due to exchange currents ($\sim 70\%$) is not observed for the IVGQR in our analysis, which gives $S_{\text{exp}} \approx 1.1 S_{\text{th}}$. Taking into account the quoted error of S_{exp}, we can estimate an upper limit for the enhancement factor of approximately 36%.

The total photoabsorption cross section and the three major contributions are shown in the right panel of figure 6 in comparison with the compilation of Varlamov *et al.* [32].

With these ingredients, we may also calculate the energy spectra of all the evaporated protons using the relation:

$$
\frac{d\sigma}{dT_p}(T_p, \omega) = \frac{1}{N_{\text{rep}}\langle p \rangle \Delta T_p} \frac{dN}{dT_p}(T_p, \omega)\sigma_{\gamma,\text{Sp}}(\omega), \tag{17}
$$

where N_{rep} is the number of evaporation Monte Carlo events, $\langle p \rangle$ the average proton multiplicity, ΔT_p the bin for the proton kinetic energies, and $dN/dT_p(T_p, \omega)$ the corresponding energy spectra histograms calculated in steps of ΔT_p at a given incident photon energy ω. The proton energy spectra were calculated neglecting the pre-equilibrium stage because the available data from the NBS correspond to an electron energy of 20 MeV, where the evaporation process largely dominates. The normalization (17) gives:

$$
\sigma_{\gamma,\text{Sp}}(\omega) = \int_0^{T^{\max}} \frac{d\sigma}{dT_p}(T_p, \omega) dT_p, \tag{18}
$$

with $T^{\max} = \omega - B_p$.

Because the contribution of the IVGQR decay is vanishing small at 20 MeV, we can calculate the double-differential cross section at a given electron energy weighting $d\sigma/dT_p(\omega, T_p)$ with the $E1$ virtual photon spectrum:

$$
\begin{aligned}
&\frac{d^2\sigma}{d\Omega_p dT_p}(T_p, E_e) \\
&= \frac{1}{4\pi} \int_{B_p}^{E_e} \frac{d\omega}{\omega} S^{E1}(E_e, \omega)\frac{d\sigma}{dT_p}(T_p, \omega), \tag{19}
\end{aligned}
$$

where we have assumed an isotropic angular distribution for the emitted protons. So, inserting Eq. (17) into Eq. (19), we can calculate the double-differential cross section $(d^2\sigma/dT_p d\Omega)(T_p, E_e)$. The results are presented in Fig. 7, together with the NBS data obtained at $\theta_p = 90°$ with $E_e = 20$ MeV. The calculation reproduces reasonably well the overall shape of the spectrum, except for the sharp structures around the peak. It should be considered, however, that the MCMC model is not intended to reproduce these structures, which are associated with some specific and well-established excited states of ^{89}Y. In fact, the MCMC calculation is intended to describe the average behavior of the nuclear reaction mechanism in a wide energy and target mass range and few peculiarities − related with a given mass domain − are
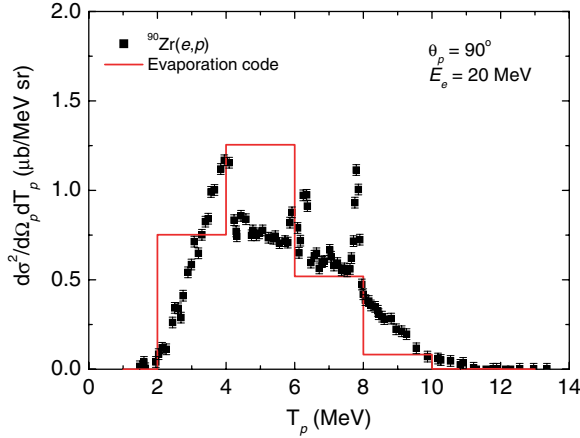
FIG. 7. (Color online) Double-differential energy spectra of protons emitted at 90° for an incident electron energy of 20 MeV [10](data points). The red histogram is the prediction of Eq. (19) (evaporation only).

introduced in terms of the nuclear level density parameters and shell-model corrections.

C. Photoneutron cross sections from threshold to 140 MeV

In the previous section, we have shown that the MCMC plus evaporation cascade reproduces quite successfully the precise measurements of the electrodisintegration proton yield from the NBS [10]. However, for the sake of completeness, we should also verify the efficiency of the Monte Carlo approach in reproducing the photoneutron cross section measurements on ^{90}Zr performed at Livermore [11] and Saclay [12]. These data are related with the $(\gamma, 1n) = (\gamma, n) + (\gamma, np)$ and $(\gamma, 2n) = (\gamma, 2n) + (\gamma, 2np)$ channels, which represent the major fraction of the total photoabsorption cross section below approximately 30 MeV.

For energies above the GDR region, there is just one data set available from Saclay [14]. These data consist of the inclusive partial and total photoneutron cross sections from natural Zirconium up to 134 MeV, where they have reported neutron multiplicities with reasonable statistics up to seven particles. These measurements represent the only data set of multiple-particle emissions followed by intermediate energy photoabsorption in this mass region and should be interpreted in terms of the MCMC model via the QD photoabsorption mechanism.

Before we compare the predictions of the MCMC cascade with the data from Livermore and Saclay, it is important to establish a consistent method to overcome the systematic discrepancies between the absolute cross section measurements [25,28]. This can be achieved by comparing the total integrated photoneutron yield of ^{90}Zr from Livermore and Saclay with the prediction of the MCMC model, which is given by:

$$\sigma_{\gamma,\text{Sn}}^{\text{int}}(E_\gamma^{\text{max}}) = \int_{B_n}^{E_\gamma^{\text{max}}} \sigma_{\gamma,\text{Sn}}(\omega)d\omega, \quad (20)$$

where

$$\sigma_{\gamma,\text{Sn}}(\omega) = [C_0\sigma_{\text{GDR}}(\omega) + C_1\sigma_{\text{IVGQR}}(\omega)]$$
$$\times \Gamma_{\gamma,\text{Sn}}^R(\omega) + \sigma_{\text{QD}}(\omega) \times \Gamma_{\gamma,\text{Sn}}^{\text{QD}}(\omega). \quad (21)$$

The contribution $C_0\sigma_{\text{GDR}}(\omega)$ and the constants C_1 and C_2 were obtained in the previous section using the NBS measurements, whereas the branching ratios $\Gamma_{\gamma,\text{Sn}}^{R(\text{QD})}(\omega)$ are calculated within the MCMC routine. So, the normalization factors between the Livermore $N_{(L)}$ and Sacaly $N_{(S)}$ data and the NBS data can be written as:

$$N_{(L)\text{ or }(S)} = \frac{\sigma_{\gamma,\text{Sn}}^{\text{int}}\left(E_\gamma^{\text{max}(L)\text{ or }(S)}\right)}{\sigma_{\gamma,\text{Sn}}^{\text{int}(L)\text{ or }(S)}}, \quad (22)$$

with $\sigma_{\gamma,\text{Sn}}^{\text{int}(L)} = 1158$ MeV.mb, $\sigma_{\gamma,\text{Sn}}^{\text{int}(S)} = 1309$ MeV.mb, $E_\gamma^{\text{max}(L)} = 27.6$ MeV, and $E_\gamma^{\text{max}(S)} = 25.9$ MeV [30]. So, including these factors in Eq. (22), we have $N_{(L)} = 1.097$ and $N_{(S)} = 0.917$, with $N_{(L)} \times N_{(S)} = 1.005$. This result indicates that the NBS data lie around the average between the photoneutron cross sections from Livermore and Saclay. The predictions of the MCMC model for the inclusive channels $(\gamma, 1n)$ and $(\gamma, 2n)$ of ^{90}Zr can then be compared with the available measurements using the normalization constants $N_{(L)}$ and $N_{(S)}$. The results are shown in Fig. 8.

The calculation of the photoneutron cross sections up to 140 MeV was performed for the zirconium isotopes ^{90}Zr, ^{91}Zr, ^{92}Zr, and ^{94}Zr via the coupling of the MCMC and evaporation cascades. The relative isotopic composition of the target nucleus was taken into account to calculate the final cross sections for multiple neutron emission. These quantities represent the major fraction of the total photoabsorption cross
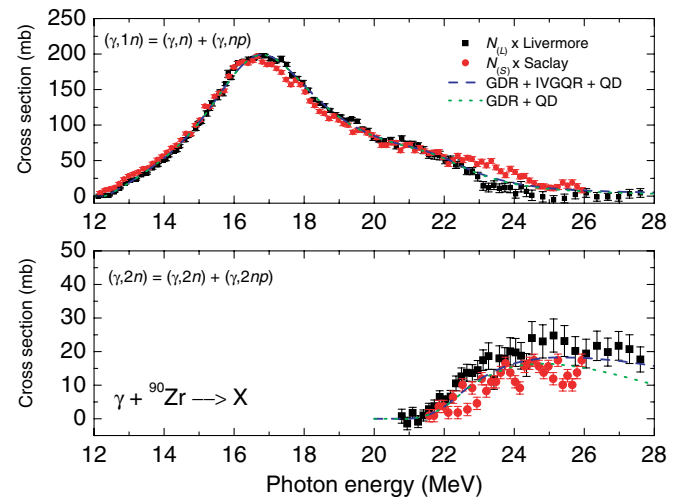

FIG. 8. (Color online) Renormalized single (upper panel) and double (lower panel) photoneutron channels on ^{90}Zr from Livermore [11] (black squares) and Saclay [12] (red circles). The dashed blue line is the prediction of the MCMC plus evaporation model taking into account the GDR, IVGQR, and QD contributions, whereas the dotted green line does not include the IVGQR decay.
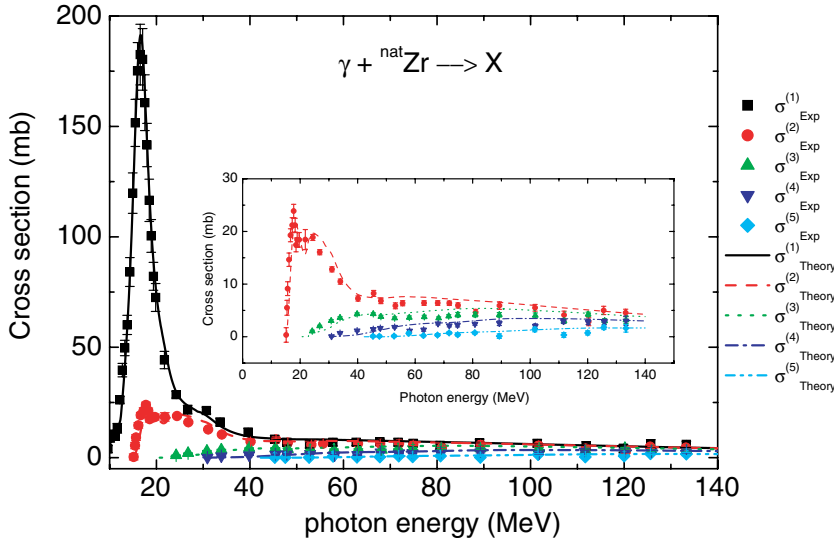
FIG. 9. (Color online) Renormalized inclusive photoneutron cross sections from Saclay [14] (data points) in comparison with the predictions of the MCMC plus evaporation calculation: $\sigma^{(1)}$ (solid black line), $\sigma^{(2)}$ (dashed red line), $\sigma^{(3)}$ (dotted green line), $\sigma^{(4)}$ (dashed-dotted blue line), and $\sigma^{(5)}$ (dashed-double-dotted cyan line). See text for details.

section and are given by:

$$\sigma^{(k)}(\omega) = \sum_{x=k}^{7} \sum_{y} \sigma_{\gamma, xnyp}(\omega). \qquad (23)$$

The results of the calculation and the Saclay data are shown in Fig. 9. The $\sigma^{(1)}(\omega)$ cross section is the total photoabsorption cross section minus the sum of all exclusive channels for charged-particle emission and photofission. The Saclay data were normalized using the constant $N_{(S)}$, being very well reproduced in shape and magnitude by the MCMC model up to 140 MeV. The insert shows the cross sections $\sigma^{(k)}(\omega)$ with $k \geqslant 2$ in a more suitable scale.

V. CONCLUSIONS AND FINAL REMARKS

The MCMC plus evaporation cascade has been successfully applied to calculate the total photoabsorption cross section and relevant decay channels of ^{90}Zr and other Zr isotopes from neutron threshold to 140 MeV. The relative strengths of the dominating GDR and the IVGQR were consistently determined for ^{90}Zr combining measurements of the proton yields—performed at the NBS—with calculations of the relevant branchings achieved by a sophisticated Monte Carlo approach. The EWSR of the IVGQR yields $S_{\mathrm{exp}} = 0.121(27)$ mb/MeV, which is in fair agreement with the theoretical value of 0.11 mb/MeV.

The decay channels of ^{90}Zr are dominated by single- and double-particle emissions (Fig. 2) up to approximately 30 MeV, with multiple-particle emissions being more relevant at higher energies. Indeed, above approximately 80 MeV, decay channels with two or more protons are more likely to occur than single-proton emission channels (Fig. 3). This fact provides an explanation for the steady increase on the electrodisintegration yield of protons reported on Ref. [10]. Such multiple proton emission scenario can be interpreted considering that at least one proton is likely to be emitted during the pre-equilibrium stage, which is in agreement with the kinematics of a photoabsorption by an n-p pair

(QD model). Two or more protons can also be emitted, because there is a high probability of secondary scatterings at these energies. So, the resulting branching ratios shown in Fig. 3 represent a combination of a pre-equilibrium part and an evaporation contribution that increases more significantly the number of emitted neutrons than protons.

The shape of the total photoabsorption cross section on ^{90}Zr was assumed to be a combination of a GDR, IVGQR, and QD contributions. The shape of the total photoabsorption cross section below approximately 30 MeV was calculated using the photoneutron yield from Livermore [11] and the branchings calculated in the MCMC model (Fig. 4). The absolute values of the cross sections were then determined via an iterative fitting procedure [Eq. (15)], combining the NBS measurements of the (e, p) yield on ^{90}Zr with the branchings of the MCMC plus evaporation. The result of the fitting is shown in Fig. 5, with the corresponding photoproton yield [Eq. (12)] being presented in Fig. 6. The total photoabsorption cross section below approximately 30 MeV was then recalculated subtracting the QD and the fitted IVGQR contributions from the fitted GDR part [Eq. (9)]. Above 30 MeV, the total photoabsorption cross section was calculated as a sum of the fitted GDR and IVGQR contributions plus the QD cross section [Eqs. (4) and (5)].

The proton energy spectrum at $E_e = 20$ MeV was calculated neglecting pre-equilibrium emissions and weighting the photoproton double-differential cross section with the $E1$ virtual photon spectrum [Eq. (19)]. The results (Fig. 7) reproduce reasonably well the trend of the experimental data of the NBS. Small discrepancies appear around the peak $T_p \sim 5$ MeV and also at higher proton energies.

The photoneutron cross sections were also calculated in the GDR region (Fig. 8). The results are in fair agreement with the measurements of Livermore and Saclay after the introduction of suitable normalization factors. These normalization constants show that the NBS data agree with the Livermore and Saclay measurements within 10%. The shapes of the $(\gamma, 1n)$ and $(\gamma, 2n)$ cross sections also reproduce the experimental results, being more compatible with the Livermore data than with those from Saclay. In fact, the Saclay $(\gamma, 2n)$ cross section presents a strong fluctuation over the whole energy

region, re-enforcing our decision of taking the Livermore measurements to shape the cross section below approximately 30 MeV.

The inclusive photoneutron cross sections of ^{nat}Zr were calculated taking into account the isotopic composition of the target nucleus. The results so obtained are in nice agreement with the normalized data set from Saclay (Fig. 9). The QD tail reproduces quite successfully all the available data up to five-neutron emissions without further normalization.

In conclusion, the MCMC plus evaporation cascade has provided a comprehensive interpretation of the behavior of the electrodisintegration yield of protons on ^{90}Zr. The results also indicate a strong evidence of a IVGQR state, leading to a realistic description of the total photoabsorption cross section in this mass range.

[1] T. E. Rodrigues, J. D. T. Arruda-Neto, A. Deppman, V. P. Likhachev, J. Mesa, C. Garcia, K. Shtejer, G. Silva, S. B. Duarte, and O. A. P. Tavares, Phys. Rev. C **69**, 064611 (2004).

[2] T. E. Rodrigues, Ph.D. thesis, University of São Paulo (2005) (unpublished).

[3] M. G. Gonçalves, S. de Pina, D. A. Lima, W. Milomen, E. L. Medeiros, and S. B. Duarte, Phys. Lett. **B406**, 1 (1997).

[4] M. G. Gonçalves, E. L. Medeiros, and S. B. Duarte, Phys. Rev. C **55**, 2625 (1997).

[5] S. de Pina, E. C. Oliveira, E. L. Medeiros, S. B. Duarte, and M. Gonçalves, Phys. Lett. **B434**, 1 (1998).

[6] S. B. Duarte (private communication).

[7] T. E. Rodrigues, J. D. T. Arruda-Neto, J. Mesa, C. Garcia, K. Shtejer, D. Dale, and I. Nakagawa, Phys. Rev. C **71**, 051603(R) (2005).

[8] B. Krusche *et al.*, Eur. Phys. J. A **22**, 277 (2004).

[9] PrimEx Proposal (http://www.jlab.org/primex/primex_notes/ PR99-014.ps, accessed in Aug-2006).

[10] W. R. Dodge, E. Hayward, M. N. Martins, and E. Wolynec, Phys. Rev. C **32**, 781 (1985).

[11] B. L. Berman, J. T. Caldwell, R. R. Harvey, M. A. Kelly, R. L. Bramblett, and S. C. Fultz, Phys. Rev. **162**, 1098 (1967).

[12] A. Leprêtre, H. Beil, R. Bergère, P. Carlos, A. Veyssière, and M. Sugawara, Nucl. Phys. **A175**, 609 (1971).

[13] M. A. Godwin, E. Hayward, G. Feldman, L. H. Kramer, H. R. Weller, and W. R. Dodge, Phys. Rev. C **50**, 1528 (1994).

[14] A. Veyssière, H. Beil, R. Bergère, P. Carlos, F. Fagot, A. Leprêtre, and A. de Miniac, Z. Phys. A **306**, 139 (1982).

[15] F. Zamani-Noor and D. S. Onley, Comput. Phys. Commun. **48**, 241 (1988).

[16] A. Boudard, J. Cugnon, S. Leray, and C. Volant, Phys. Rev. C **66**, 044615 (2002).

[17] V. F. Weisskopf, Phys. Rev. **52**, 295 (1937).

[18] A. Deppman, O. A. P. Tavares, S. B. Duarte, E. C. de Oliveira, J. D. T. Arruda-Neto, S. R. de Pina, V. P. Likhachev, O. Rodriguez, J. Mesa, and M. Gonçalves, Phys. Rev. Lett. **87**, 182701 (2001).

[19] A. Deppman, O. A. P. Tavares, S. B. Duarte, E. C. de Oliveira, J. D. T. Arruda-Neto, S. R. de Pina, V. P. Likhachev, O. Rodriguez, J. Mesa, and M. Gonçalves, Comput. Phys. Commun. **145**, 385 (2002).

[20] K. J. LeCouteur, Proc. Phys. Soc. London, Sect. A **63**, 259 (1950).

[21] W. D. Myers and W. T. Swiatecki, Nucl. Phys. **81**, 1 (1966).

[22] S. Fukuda and Y. Torizuka, Phys. Rev. Lett. **29**, 1109 (1972); H. V. Geramb, R. Sprickmann, and G. L. Strobel, Nucl. Phys. **A199**, 545 (1973); S. S. Hanna *et al.*, Phys. Rev. Lett. **32**, 114 (1974); L. L. Rutledge and J. C. Hubert, Phys. Rev. Lett. **32**, 551 (1974); S. Fukuda and Y. Torizuka, Phys. Lett. **B62**, 146 (1976).

[23] S. Krewald and J. Speth, Phys. Lett. **B52**, 295 (1974).

[24] J. S. Levinger, Phys. Rev. **84**, 43 (1951); J. S. Levinger, *Nuclear Photo-Disintegration* (Oxford University Press, Oxford, 1960); J. S. Levinger, Phys. Lett. **B82**, 181 (1979).

[25] T. E. Rodrigues, J. D. T. Arruda-Neto, Z. Carvalheiro, J. Mesa, A. Deppman, V. P. Likhachev, and M. N. Martins, Phys. Rev. C **68**, 014618 (2003).

[26] F. S. Dietrich, D. W. Heikkinen, K. A. Snover, and K. Ebisawa, Phys. Rev. Lett. **38**, 156 (1977).

[27] M. B. Chadwick, P. Oblozinský, P. E. Hodgson, and G. Reffo, Phys. Rev. C **44**, 814 (1991).

[28] J. D. T. Arruda-Neto, W. Rigolon, S. B. Herdade, and H. L. Riette, Phys. Rev. C **29**, 2399 (1984); M. N. Martins, E. Hayward, G. Lamaze, X. K. Maruyama, F. J. Schima, and E. Wolynec, Phys. Rev. C **30**, 1855 (1984); E. Wolynec and M. N. Martins, Rev. Bras. Fís. **18**, 508 (1988).

[29] J. M. Blatt and V. F. Weisskopf, *Theoretical Nuclear Physics* (Springer-Verlag, New York, 1979).

[30] S. S. Dietrich and B. L. Berman, At. Data Nucl. Data Tables **38**, 199 (1988).

[31] E. J. Williams, Phys. Rev. **45**, 729 (1934).

[32] http://www.nndc.bnl.gov/exfor3/servlet/X4sGetSubent?reqx= 2014&subID=220656013 (accessed in August 2006).